Variability in upper-ocean salinity stratification in the tropical Pacific Ocean

Wei Duan[1], Xuhua Cheng[1, 2*], Xiuhua Zhu[3], Tian Ma[1]

[1] College of Oceanography, Hohai University, Nanjing 210098, China

[2] Southern Marine Science and Engineering Guangdong Laboratory (Zhuhai), Zhuhai 519000, China

[3] Center for Earth System and Sustainability, University of Hamburg, Hamburg 20144, Germany

Abstract

Using a gridded array for real-time geostrophic oceanography (Argo) program float dataset, the features of upper-ocean salinity stratification in the tropical Pacific Ocean are studied. The salinity component of the squared Brunt-Väisälä frequency N^2 (N_S^2) is used to represent salinity stratification. Layer-max N_S^2 (LMN), defined as the N_S^2 maximum over the upper 300 m depth, and halocline depth (HD), defined as the depth where the N_S^2 maximum is located, are used to specifically describe the intensity of salinity stratification. Salinity stratification in the Topical Pacific Ocean has both spatial and temporal variability. Over the western and eastern equatorial Pacific, the LMN has a large magnitude with a shallow HD, and both have completely opposite distributions outside of the equatorial region. An obvious seasonal cycle in the LMN occurs in the north side of eastern equatorial Pacific and freshwater flux forcing dominates the seasonal variations, followed by subsurface forcing. At the eastern edge of the western Pacific warm pool around the dateline, significant interannual variation of salinity stratification occurs and is closely related to the El Niño Southern Oscillation event. When an El Niño event occurs, the precipitation anomaly freshens sea surface and the thermocline shoaling induced by the westerly wind anomaly lifts salty water upward, together contribute to the positive salinity stratification anomaly over the eastern edge of the warm pool. The interannual variations in ocean stratification can slightly affect the propagation of first baroclinic gravity waves.

Key words: Brunt-Väisälä frequency, salinity stratification, seasonal and interannual variations, gravity wave

1 Introduction

The tropical Pacific Ocean (TPO) is an extremely important component of the global ocean. Both the Intertropical Convergence Zone (ITCZ) and the South Pacific Convergence Zone (SP-CZ) are located in the TPO, and they together form the largest rainfall center in the world. Precipitation can largely affect ocean property by changing upper-ocean salinity. The associated variability in upper-ocean salinity and its impact on ocean-atmosphere interactions have been studied extensively. As a crucial property of ocean, salinity can be a good tracer for investigating ocean dynamic processes. Additionally, as an important component of the global water cycle, ocean salinity can act as a rain gauge (Alory et al., 2012; Yu, 2011) and indicate the budget of ocean freshwater.

Compared with the large number of temperature observations, field observation data of ocean salinity are relatively scarce, which has led to the long-term lack of research on ocean salinity. This situation has been substantially changed recently. With the successful launch and operation of salinity exploration satellites, such as Aquarius by the National Aeronautics and Space Administration (NASA) (Lagerloef et al., 2008), soil moisture and ocean salinity (SMOS) by the European Space Agency (ESA) (Font et al.,

2010) and Soil Moisture Active Passive (SMAP) L-band microwave onboard radiometer by NASA (Entekhabi et al., 2010), multiscale variations of sea surface salinity (SSS) now can be investigated in detail. Moreover, the Array for Real-time Geostrophic Oceanography (Argo) program, which began from the early 21st century, collected ocean salinity from surface to deep ocean and has been running for more than 16 years, which is much longer than other satellite program (Roemmich et al., 2009). With the extension of temporal and spatial distributions of the Argo profiles, scientists now have a better opportunity to understand the 3D structures of ocean salinity.

Many previous studies have already described the sea surface salinity (SSS) variability at seasonal, interannual and decadal time scales in the TPO. A dramatic SSS front around the eastern edge of the western Pacific warm pool has been discussed in previous studies (Bosc et al., 2009; Delcroix and Hénin, 1991; Delcroix and McPhaden, 2002; Qu et al., 2014; Qu and Yu, 2014; Singh et al., 2011). The SSS front moves zonally at interannual timescales associated with the El Niño Southern Oscillation (ENSO) (Bosc et al., 2009; Qu et al., 2014; Qu and Yu, 2014), and its longitudinal location can capture the ENSO signal; thus, it can be a new index to identify types of El Niño events (Qu and Yu, 2014).

*Corresponding author, E-mail: xuhuacheng@hhu.edu.cn

Zhi et al. (2019c) showed that the salinity results differed between two extreme El Niño and one weak El Niño in the western-central equatorial Pacific. Zhi et al. (2019b) revealed that the observed mixed layer salinity tendency leads El Niño by 12 months due to the influence of freshwater flux. Guan et al. (2019) suggested that a dipole structure of mixed layer salinity in the western-central equatorial Pacific is a characteristic of El Niño-La Niña asymmetry. In addition to the western part of the equatorial Pacific, salinity fronts also occur under the boundary of the ITCZ and the eastern Pacific fresh pool (Kao and Lagerloef, 2015). The long-term trend of the SSS has also been investigated by previous studies. Du et al. (2015) revealed that there is a significantly increasing salinity trend in the western tropical Pacific during 2004–2014 based on Argo float data and they indicated that the intensification of the Walker circulation accounted for this SSS trend. Under a climate change background, Du et al. (2019) evaluated the close relationship between SSS and climate change under the condition of global warming and its recent hiatus.

Vertical salinity stratification in the Pacific Ocean has been a focus of ocean scientists as well. A number of studies have demonstrated that strong salinity stratification exists on the west side of the western Pacific warm pool SSS front, and it can generate a thick barrier layer (Luka and Lindstrom, 1991; Sprintall and Tomczak, 1992; Vialard and Delecluse, 1998; Wang and Liu, 2016). The variability in barrier layer thickness (BLT) is a hot research issue since it can influence air-sea interactions by trapping both heat and momentum in a shallow layer (Godfrey and Lindstrom, 1989). Salinity stratification can also be linked to ocean dynamic processes. Chen et al. (2018) indicated that the annual amplitude and phase of subsurface salinity show an obvious signal in the equatorial current system and wave propagation. Zhi et al. (2019a) investigated the warm "Blob" in the northeastern Pacific during the winter of 2013/2014 and they suggested that salinity variability accounted for about 60% of the mixed layer depth (MLD) shoaling. Previous studies have also found that subsurface salinity usually presents a similar response to El Niño events as SSS. The strong freshwater anomaly during the 2015/2016 El Niño (Gasparin and Roemmich, 2016) and the reason for the failed 2014/2015 El Niño (Chi et al., 2019) can be properly explained by salinity under the surface.

Vertical stratification or vertical stability of the ocean was originally quantified by the gradient of density. However, previous researchers have noted that it is not suitable to define the vertical stability of the water column by using only the vertical gradient of potential density (e.g., McDougall, 1987). Currently, the squared Brunt-Väisälä frequency N^2 is primarily used to describe ocean stratification, and it has been widely applied in many studies. Helber et al. (2012) estimated the transition layer thickness as the distance between the mixed layer depth and the deepest N^2 value, which is equal to half of the maximum N^2 that occurs in the profile. In Maes (2008), a method was proposed that makes use of the dependency of the squared Brunt-Väisälä frequency $N^2(T, S)$. By separating the impact of temperature from N^2, the layer where salinity stratification plays a key role in N^2 can be isolated. This method has been applied in other studies by dividing N^2 into N_S^2 and N_T^2. Zheng and Zhang (2012) indicated that during the 2007/2008 La Niña event, the positive salinity anomaly in the western-central Pacific played a more significant role than negative temperature anomaly in destabilizing the upper layers. Maes and O'Kane (2014) identified global seasonal variability in ocean salinity stratification (OSS as defined by the upper-300 m averaged positive N_S^2) and illustrated that regions without permanent barrier layer may also existing strong salinity stratific-

ation (large OSS). Guimbard et al. (2017) explained that N_S^2 can better explain the shoal of pycnocline than N_T^2 in the 2014/2015 rainy seasons over the central equatorial Pacific. Moreover, the role of N^2 variability on the baroclinic Rossby radius (λ) was studied by Chelton et al. (1998), and they found that changes of N^2 had a limited contribution toward λ(1%–2%) at seasonal time scale.

The upper-ocean mixed layer is where air-sea interactions occur. At the base of the mixed layer, temperature or salinity changes rapidly with depth, leading to a large vertical gradient. Isothermal/isohaline layer depth, or the thermocline/halocline depth, is defined as the depth where temperature/salinity changes quickly. Many important oceanic physical processes occur in the thermocline, such as internal waves. The depth of the thermocline has received much attention, but an accurate definition of thermocline depth is still disputed. Many previous studies have been performed to determine the best method to define the thermocline depth specifically and quantify the thermocline depth. Luka and Lindstrom (1991) used a temperature gradient criterion of 0.05°C/m for the top of the thermocline. Sprintall and Tomczak (1992) fixed the thermocline depth as a temperature threshold of 0.5°C. Lorbacher et al. (2006) used the curvature criterion to define the thermocline depth. Chu and Fan (2011) provided a maximum angle method to determine the mixed/isothermal layer depth.

Compared to the thermocline, the isohaline layer depth (or halocline depth) has received less attention. The lack of salinity data and the view that salinity is not crucial to determining ocean properties are responsible for the lack of research. Helber et al. (2012) defined the isohaline layer depth as a salinity threshold that is equal to a density increase of 0.2°C. This method is applicable when temperature and salinity data are sufficient, but complexities make it difficult to be widely used.

It is well known that the salinity stratification in TPO play an important role in the ocean dynamics and air-sea interaction. However, most of previous studies on salinity stratification are mainly focused on the barrier layer in the western Pacific warm pool (Bosc et al., 2009; Godfrey and Lindstrom, 1989; Luka and Lindstrom, 1991; Sprintall and Tomczak, 1992; Vialard and Delecluse, 1998; Wang and Liu, 2016). Additional studies about variability in salinity stratification are focused on the upper-layer averaged N_S^2 (Maes, 2008; Maes and O'Kane, 2014; O'Kane et al., 2016), with either rare data or different regional extent. So to date, the temporal and spatial variations in upper-ocean salinity stratification in the TPO, as well as the related mechanisms, have not been fully studied. 16 years of Argo observations are available, which can be used to reveal the variability in salinity stratification accurately.

In this study, the magnitude and the depth location of the maximum N_S^2 over the upper layer are used to specifically describe the intensity of salinity stratification, which is believed to be a new thought from previous studies. The main purpose of this study is to describe the spatial and temporal variability of upper ocean salinity stratification in the TPO and mechanisms control these variations. The content of this manuscript is arranged into five sections. Section 2 describes the data and methodology; Section 3 describes the observed climatological features of several physical phenomena; Section 4 describes the salinity stratification variations, summarizes the main seasonal-interannual features of other relatively well-known climatic variables, identifies their contributions to salinity stratification and shows the interannual variability in 1st baroclinic gravity-wave phase speed; and Section 5 summarizes and discusses the main results.

2 Data and methodology

2.1 *Data*

The development of the Argo program in the early 21st century provided us with a good opportunity to study ocean stratification, especially for salinity stratification. In this investigation, 14 years (January 2004 through December 2017) of gridded Argo temperature and salinity data were obtained from the China Argo Real-Time Data Center, and this dataset is named BOA_Argo (Lu et al., 2020). There are 58 vertical layers in the dataset, and they range from the sea surface to a depth of 2 000 m (vertical resolution ranging from 10 m between the surface and a depth of 200 m to 100 m between depths of 1 700 m and 1 975 m), with an interpolated spatial resolution of 1°× 1° and a monthly temporal resolution. An original PROVOR Argo float located at (2.4°S, 170.7°E) on 26 September 2013 was employed. World Ocean Atlas 2013 (WOA13) version 2 seasonal climatology temperature and salinity data are used as well.

The ERA-Interim synoptic monthly mean 10-m wind field data from the European Centre for medium-range weather forecasts (ECMWF) are used (Simmons et al., 2006). Precipitation data are from the Global Precipitation Climatology Project (GPCP) version 2.3 (Adler et al., 2018). Evaporation data are derived from the Woods Hole Oceanographic Institution (WHOI) objectively analyzed air-sea flux (OAFlux) version 3 monthly dataset (Yu et al., 2008). Surface current data are from the ocean surface currents analyses real-time (OSCAR) one third degree resolution ocean surface currents dataset, version 2009 (Bonjean and Lagerloef, 2002). All datasets are processed at a 1°× 1° spatial resolution and a monthly temporal resolution.

2.2 *Analyses*

2.2.1 *Mixed-layer salinity budget*

The mixed-layer salinity budget combines the works of Feng et al. (1998), Yu (2011) and Hasson et al. (2013) and is used to diagnose the variation in salinity:

$$\frac{\partial S}{\partial t} = -\left(u\frac{\partial S}{\partial x} + v\frac{\partial S}{\partial y}\right) - \frac{S_0\,(P-E)}{h} - w_e\frac{S - S_{-h}}{h} + \kappa\nabla^2 S, \quad (1)$$

where S_0 represents the surface salinity, u and v represent the surface zonal and meridional currents, h represents the mixed layer depth, w_e represents the Ekman pumping velocity, S_{-h} represents the salinity at the base of the mixed layer, and κ represents the diffusion coefficient.

The left-hand side of Eq. (1) gives the temporal variation in mixed layer salinity. The first term on the right-hand side is the advection term or the salt transport term due to the surface current. The second term on the right-hand side is the freshwater forcing term due to precipitation and evaporation. The last two terms on the right-hand side show the vertical entrainment and diffusion terms, which are considered together as subsurface forcing (Hasson et al., 2013; Zhi et al., 2019b). Here, the mixed layer depth (denoted by h) is defined as the minimum of the isopycnal layer depth and the isothermal layer depth with a temperature threshold of 0.5°C (Sprintall and Tomczak, 1992). In this mixed layer salinity equation, the effect of river runoff is not considered.

2.2.2 *Salinity stratification*

In this study, temperature and salinity components in squared Brunt-Väisälä frequency N^2 were separated, following Maes (2008), and attention was mostly focused on N_S^2. The methods used to calculate N_S^2 are as follows:

$$N^2 = g\alpha T_z - g\beta S_z = N_T^2 + N_S^2, \quad (2)$$

$$N_T^2 = g\alpha T_z, \quad (3)$$

$$N_S^2 = -g\beta S_z, \quad (4)$$

where g represents the gravity acceleration; α represents the thermal expansion coefficient, which expresses the change in density for a given change in temperature; β represents the haline contraction coefficient, which expresses the change in density for a given change in salinity; T_z represents the vertical temperature gradient; S_z represents the vertical salinity gradient.

Figure 1 gives the profile of salinity, g, β, $\mathrm{d}S/\mathrm{d}z$ and N_S^2 by a PROVOR Argo float located at (2.4°S, 170.7°E) on 26 September
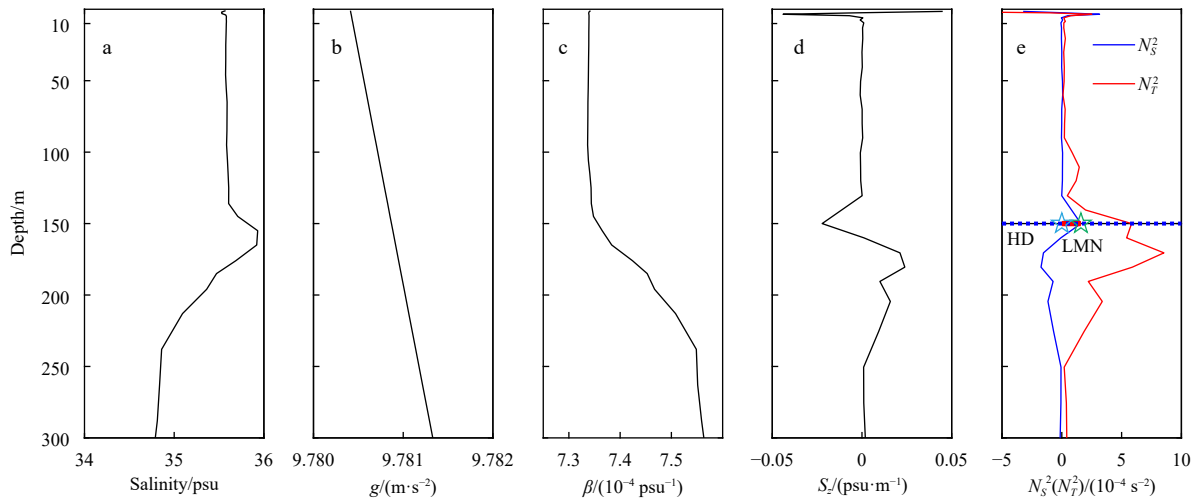
Fig. 1. Vertical profiles of salinity (a), g (b), β(c), $\dfrac{\mathrm{d}S}{\mathrm{d}z}$ (d) and N_S^2 and N_T^2 (e) from a single PROVOR Argo float located at (2.4°S, 170.7°E) on 26 September 2013. Blue dotted line in e indicates the halocline depth (HD) and magnitude between two asteroidal marks in e shows the layer-max N_s^2 (LMN).

2013. Salinity is nearly uniform in the upper 135 m and then increases to a maximum at a depth of 165 m and after that, salinity begin to decrease with increases of depth (Fig. 1a). Both the gravity acceleration g and haline contraction coefficient β increase with increases of depth (Figs 1b and c). The vertical gradient of salinity ($\mathrm{d}S/\mathrm{d}z$) shows substantial noises in the upper few meters (Fig. 1d). To avoid diurnal salinity variations near the surface due to precipitation or river discharge, in this study, the top reference level of the computation is mostly fixed at a depth of 10 m. There is a negative value of $\mathrm{d}S/\mathrm{d}z$ between 130 m and 160 m, which indicates a salinity-stratified layer, while a positive value of $\mathrm{d}S/\mathrm{d}z$ exists below 160 m, where salinity plays a role in destabilization. The profile of N_S^2 is basically opposite to that of $\mathrm{d}S/\mathrm{d}z$ (Fig. 1e), so positive N_S^2 (130–160 m) shows the salinity-stratified layer. According to the definition, the halocline depth (HD) is the depth where salinity changes fastest vertically. Since N_S^2 can represent the vertical gradient of salinity, the depth where N_S^2 reaches its maximum is defined as HD. The magnitude of N_S^2 at HD is named as the layer-max N_S^2 (LMN) since it represents the maximum value of N_S^2 in the upper-layer (0–300 m in this study).

N_S^2 is consisting of three parts: the gravity acceleration g, the haline contraction coefficient β and the salinity gradient ($\mathrm{d}S/\mathrm{d}z$). Amplitude of variations in g and β in the upper 300 m is about 0.001 m/s^2 and 0.000 02 psu^{-1}, respectively (Figs 1b and c). Among them, only β is affected by temperature. The impact of temperature variability on β is very small, which indicates the contribution of temperature to N_S^2 can be neglected. The relation between N_S^2 and $\mathrm{d}S/\mathrm{d}z$ is approximately linear. In Fig. 1e the profile of N_T^2 is shown as well. It can be observed that temperature stratification is larger than salinity stratification, or to say that the

temperature contributes more to the total stratification than salinity. Their respective contribution can be estimated by the magnitude of N_S^2 and N_T^2. Compared with $\mathrm{d}S/\mathrm{d}z$, N_S^2 is more appropriate to quantificationally describe the ocean salinity stratification, which can be also used to estimate its contribution to total stratification.

3 Climatology

3.1 *Horizontal and vertical distributions of salinity*

A salinity discrepancy between the southern and northern tropical Pacific can be observed at all levels, with saltier water in the south and fresher water in the north (Fig. 2). At the surface level, the wind-evaporation-SST (WES) positive feedback process maintains the climatological position of the ITCZ north of the equator (Xie, 1999, 2004), and the accompanying heavy rainfall in the ITCZ reduces salinity at the ocean surface north of the equator. Along the continental coasts of Central American continental coast, river runoff associated with coastal rains contributes approximately 30% of the freshwater inputs to the ocean (Alory et al., 2012). For the subsurface ocean, the maximum salinity center systematically migrates westward along with depth by the joint role of subtropical gyres and mesoscale eddies (Chen et al., 2018). South Pacific tropical water (SPTW) can subduct equatorward through the western boundary or through the interior pathway and form salty water at surface and subsurface of equatorial region (Qu et al., 2013).

Figure 3 shows the horizontal distribution of N_S^2 at different depths during 2004–2017. There is a relatively weaker hemispheric discrepancy than that of salinity. With the climatological posi-
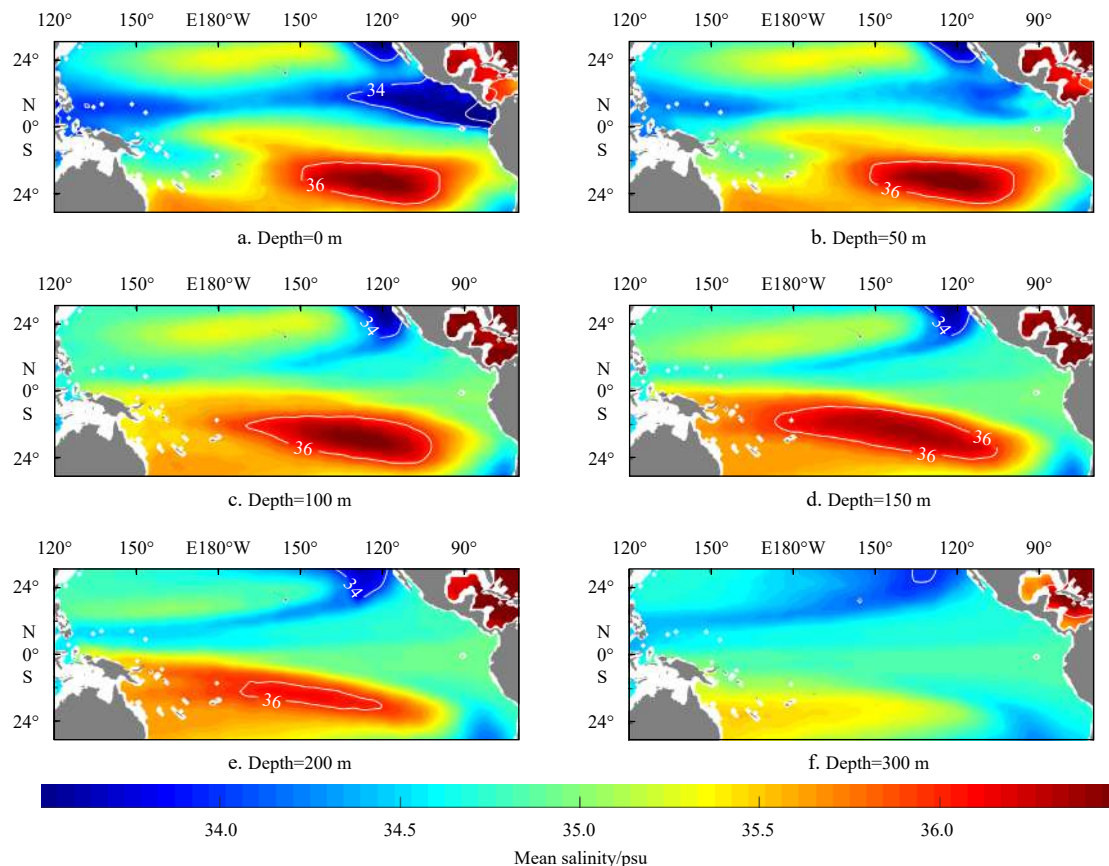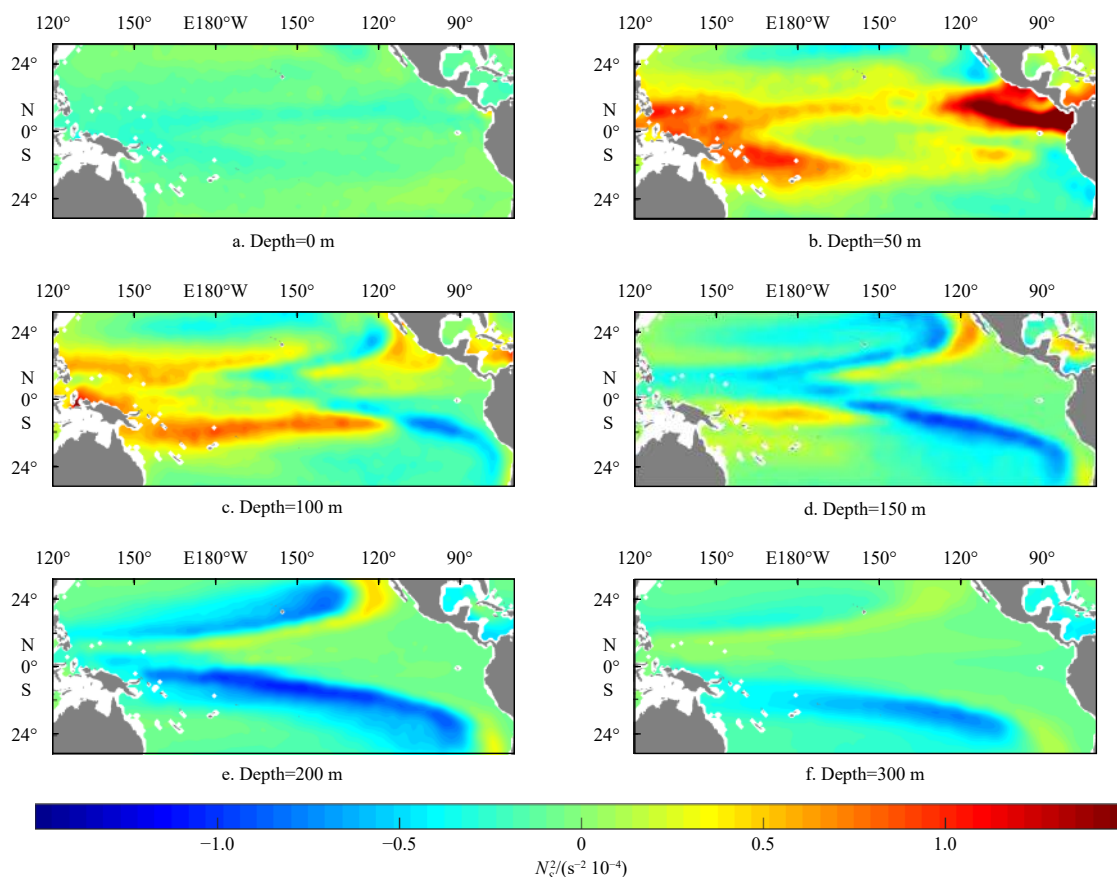

Fig. 2. Long-term (2004–2017) mean salinity distribution at depths of 0 m (a), 50 m (b), 100 m (c), 150 m (d), 200 m (e) and 300 m (f).

Fig. 3. Long-term (2004–2017) mean N_S^2 distribution at depths of 5 m (a), 50 m (b), 100 m (c), 150 m (d), 200 m (e) and 300 m (f).

tion of the ITCZ north of the equator, the N_S^2 value in the Northern Hemisphere is larger than that in the Southern Hemisphere at the surface layer. N_S^2 reaches its maximum at a depth of approximately 50 m in the eastern Pacific and approximately 50–100 m in the western Pacific (Figs 3b and c). The magnitude of N_S^2 is particularly large in the western and eastern equatorial Pacific compared to other regions. Outside the equator below the maximum N_S^2 depth, considerable negative N_S^2 values exist, which indicates the unstable salinity layer (Figs 3d–f).

The vertical distribution of salinity along the equator (2.5°S–2.5°N) is shown in Fig. 4a. The maximum salinity is located at approximately 150 m in the western equatorial Pacific and gradually shoals to 100 m in the eastern region (black line in Fig. 4a). In the western equatorial Pacific, a water mass saltier than 35.4 psu exists under the surface fresh water. This salty water mass creates very strong salinity stratification upward and negative salinity stratification below (Fig. 4b). In the central equatorial Pacific, isohaline outcrops around the dateline and salinity stratification are relatively weak. The isohaline outcrop is believed to have a great impact on water mass exchange between the central and western Pacific by subducting salty water from the central Pacific to the subsurface of the warm pool (Bosc et al., 2009; Luka and Lindstrom, 1991; Wang and Liu, 2016). In the eastern equatorial Pacific, fresh water is limited to a shallower layer.

Figure 4b shows the vertical distribution of N_S^2 along the equator (2.5°S–2.5°N). Large N_S^2 exists in the upper 100 m of western equatorial Pacific and in the upper 50 m of eastern equatorial Pacific, which indicates very strong salinity stratification. Contours of the ratio of N_S^2 over N^2 are superimposed in Fig. 4b,

which indicates the significance of salinity stratification over the total ocean stratification. Salinity stratification plays a very important role in the upper l00 m layer in the western equatorial Pacific, where N_S^2/N^2 is large. When N_S^2/N^2 exceeds 50%, the contribution of salinity stratification is larger than that of temperature stratification in a sense.

Salinity has large amplitude of variations in the upper layer of western equatorial Pacific and eastern equatorial Pacific, with standard deviation of approximate 0.4 psu (Fig. 4c). The spatial pattern of the standard deviation in N_S^2 along the equator has some discrepancy to that of salinity (Fig. 4d). For example, in the upper layer (10–30 m) of western equatorial Pacific where salinity has large STD, N_S^2 has relatively small STD compare with the layer beneath it. The reason for this difference is that mixed layer depth is mostly deeper than 30 m in this region. Salinity in the mixed layer varies synchronously so its vertical gradient changes slightly.

3.2 *Climatological means of the LMN and HD*

LMN and HD, which were defined in Section 2, were calculated using gridded Argo data. The climatological magnitude of the LMN shows a strong spatial difference (Fig. 5a). In the eastern Pacific fresh pool (EPFP) and western Pacific warm pool (WPWP) with small SSS, the LMN is larger than it is in other regions. The LMN is extremely large in the EPFP, which is associated with very fresh surface water (<34 psu, Fig. 2). In the subtropical gyre outside the rainfall zone, the LMN becomes very small. In contrast, the HD is deep outside the equatorial region and shallow within the equatorial region (Fig. 5c). In the north-
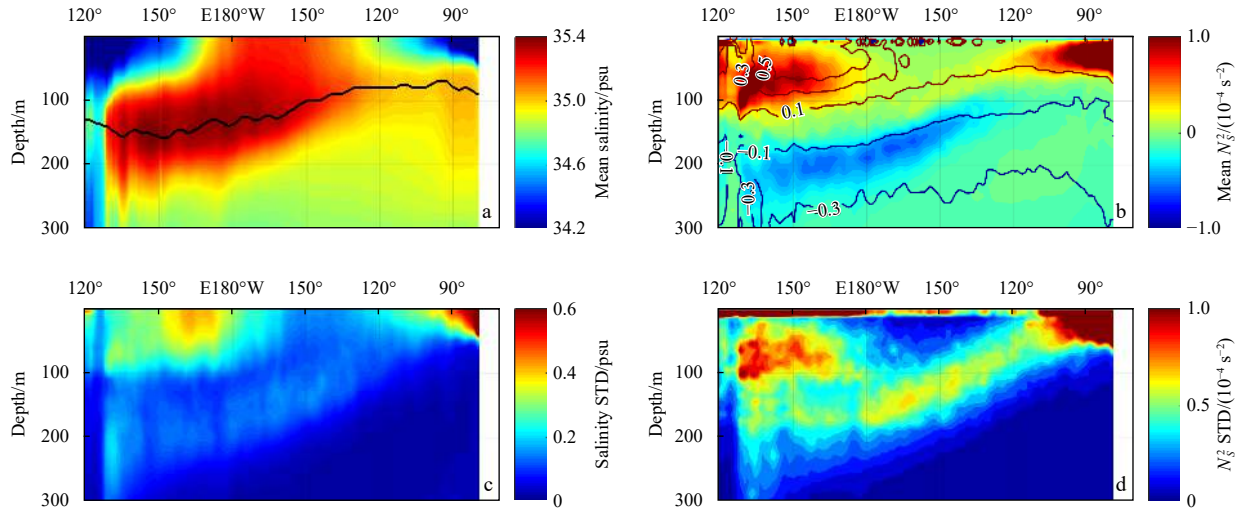
Fig. 4. Long-term (2004–2017) mean salinity distribution (a), long-term (2004–2017) mean N_S^2 distribution (b), distribution of the standard deviation of salinity (c) and distribution of the standard deviation of N_S^2 (d) within the equatorial band (2.5°S–2.5°N). Contours are superimposed in b using the ratio of N_S^2 over N^2. Black line in a indicates the depth where salinity maximum locates.
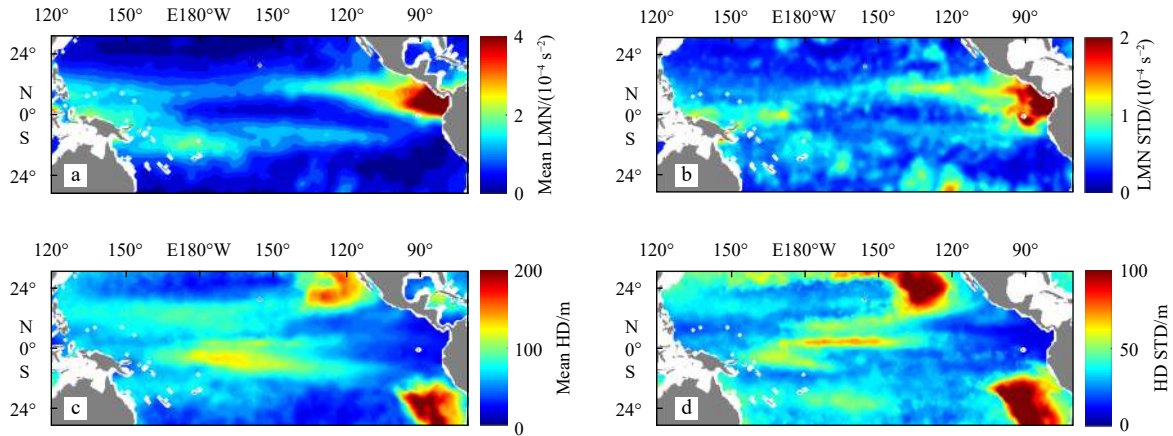
Fig. 5. Spatial distributions of the long-term mean LMN (a), standard deviation of the LMN (b), long-term mean HD (c) and standard deviation of HD (d) during 2004–2017.

east and southeast subtropical Pacific, the LMN is close to 0, and HD can be deeper than 150 m.

Maes and O'Kane (2014) have revealed the seasonal variability in positive upper-layer averaged N_S^2, which is defined as OSS. The variability in the LMN and the depth where the LMN is located have received less attention. The standard deviations (STD) of the LMN and HD are presented in Figs 5b and d, respectively. STD of both LMN and HD are proportional to their long-term mean values to a large extent, as the spatial patterns of their STD are similar to those of long-term mean. The STD of the LMN is approximately half of its mean value over the WPWP and EPFP. With the existence of a thick barrier layer over the WPWP and large freshwater input over the EPFP, the mechanism that controls the variations in the LMN in the eastern and western sides may be different. In the northeast and southeast subtropical Pacific, the HD has a large magnitude of STD, and in these areas associated with a very small LMN, a slight variation in salinity accounts for a large fraction, resulting in a sensitive change in HD.

### 3.3 *Climatological oceanic and atmospheric physics*

Figure 6a shows the spatial distribution of climatological

mean evaporation (OAFlux) minus precipitation (GPCP). It is evident that regions with large LMN and shallow HD fit well with the positions of the ITCZ and SPCZ, where large amounts of precipitation exceed evaporation. Heavy rainfall stabilizes the upper layer and increases the N_S^2 in a shallow layer, so large precipitation capacity in these regions is responsible for these distributions to a great extent. Over the EPFP, the coastal rain near the Cordillera can flow along the coastal mountain slop and bring freshwater to the ocean (Alory et al., 2012). Outside the rainfall zone, evaporation instead of precipitation dominates the distribution of salinity, thus forming salty surface water, weakening the salinity stratification and then creating a region with small LMN and deep HD, especially in the southeast and northeast tropical Pacific (Fig. 5). Freshwater forcing term in Eq. (1) $\left(-\dfrac{S_0\,(P-E)}{h}\right)$ shows the magnitude of ocean salinity variations induced by freshwater flux. The climatological spatial pattern of the freshwater forcing term is similar to that of *E–P* (Fig. 6b).

The spatial distribution of the climatological mean OSCAR surface currents is shown in Fig. 7a. The main current system in this region includes the westward North Equatorial Current,
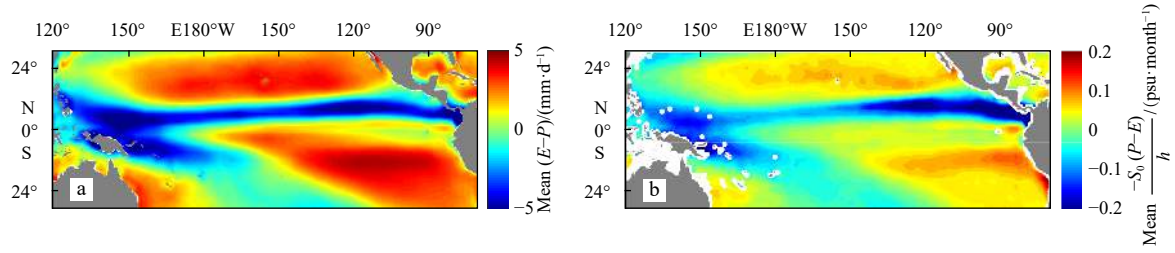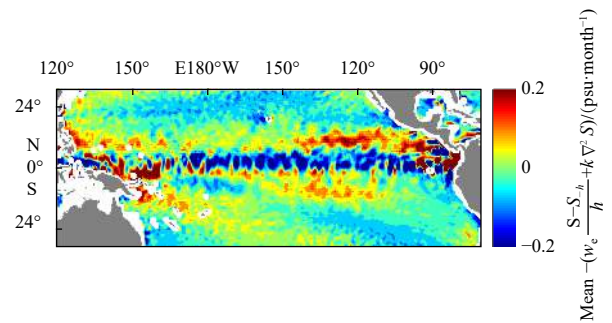
Fig. 6. Spatial distribution of the climatological mean OAFlux evaporation minus GPCP precipitation (E–P) (a) and climatological mean freshwater flux term in Eq. (1) $\left(-\dfrac{S_0\,(P-E)}{h} \right)$ (b).
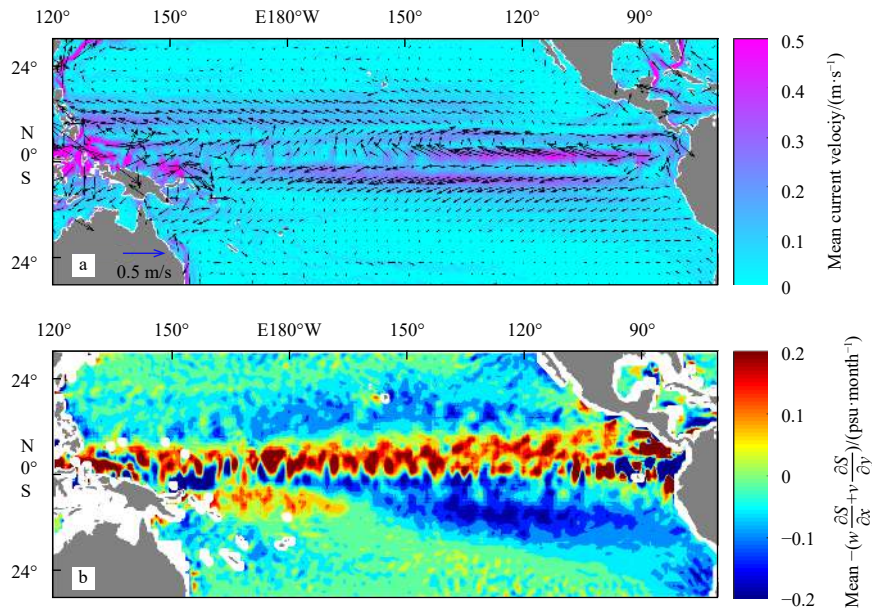
Fig. 7. Spatial distribution of the climatological mean OSCAR current field (shading: current velocity) (a) and climatological mean horizontal advection term in Eq. (1) $\left(-\left(u\dfrac{\partial S}{\partial x} + v\dfrac{\partial S}{\partial y} \right) \right)$ (b).

South Equatorial Current and eastward North Equatorial Countercurrent, which are well presented. Most of strong currents with large velocity are limited in the equatorial region (10°S–10°N). The horizontal advection term in Eq. (1) $\left(-\left(u\dfrac{\partial S}{\partial x} + v\dfrac{\partial S}{\partial y} \right) \right)$ is shown in Fig. 7b. Generally, there is a latitude band with a tendency of salinity to increase slightly north of the equator (near 5°N) and a tendency of salinity to decrease on both the north and south sides of this latitudinal band. This latitudinal band coincides well with the climatological position of the ITCZ (Fig. 6a). It is evident from Fig. 2a that the meridional gradients of salinity between this band and its northern/southern side are large. With surface currents moving in a poleward direction in this latitudinal band, freshwater can be transported to the north and south sides of the band. The magnitude of horizontal advection term is comparable to that of the freshwater forcing term, indicating that the advection term also plays an important role in the salinity budget, especially around the equator.

Following Hasson et al. (2013), who considered the term on the left-hand side of Eq. (1) to be zero for the mean state, the subsurface forcing term is then the residual value of the freshwater flux term and advection term. The mean subsurface forcing term $\left(-w_e\dfrac{S-S_{-h}}{h} + \kappa\nabla^2 S \right)$ is equal or even more important than the

Fig. 8. Spatial distribution of the climatological mean subsurface forcing term in Eq. (1) $\left(-w_e\dfrac{S-S_{-h}}{h} + \kappa\nabla^2 S \right)$.

other two terms (Fig. 8).

4 Seasonal-to-interannual variability

4.1 *Seasonal cycle*

A harmonic analysis is used to investigate seasonal variations in the LMN during the period of 2004–2017 (Fig. 9). The annual

amplitude is close to the standard deviation of the LMN, which indicates the importance of annual variations among the total variations in the LMN. The strongest annual variability is located over the north side of eastern equatorial Pacific (Fig. 9a, Region A, 6°–16°N, 145°–90°W) where both the mean value and standard deviation of the LMN are significant. A moderate annual signal can also be observed over the south side of eastern equatorial Pacific Ocean (Fig. 9a, Region B, 10°–3°S, 118°–88°W). The semiannual amplitude of LMN is less than half of the annual amplitude in most regions (Fig. 9b). It should be mentioned that both the annual and semiannual amplitudes are especially large in the Panama Bight (blue box in Figs 9a and b, 1°S–9°N, 88°–78°W). With the existence of Panama gap wind (Xie et al., 2005), monsoon rainfall and river discharge (Alory et al., 2012), dynamics in this region may be very complex and multiscale. These processes are beyond the scope of this discussion and will be investigated

in the future.

Figure 9c shows the annual phase of the LMN. There is an obvious difference in the annual phase between the eastern and western equatorial Pacific. The LMN reaches its peak value in March–April over the eastern equatorial region and in September–December over the western equatorial region and the ITCZ. In terms of the semiannual phase, a phase difference of approximately 3 months between the western and eastern equatorial Pacific can be well identified (Fig. 9d).

To better understand the specific seasonal evolution of salinity stratification and its related physical mechanisms, April, July, October and January are used to represent boreal spring, summer, autumn and winter, respectively. Figure 10 shows the spatial distribution of LMN anomaly relative to its long-term mean value in aforementioned four months. The most discernible features of the LMN anomaly occur in boreal spring and autumn,
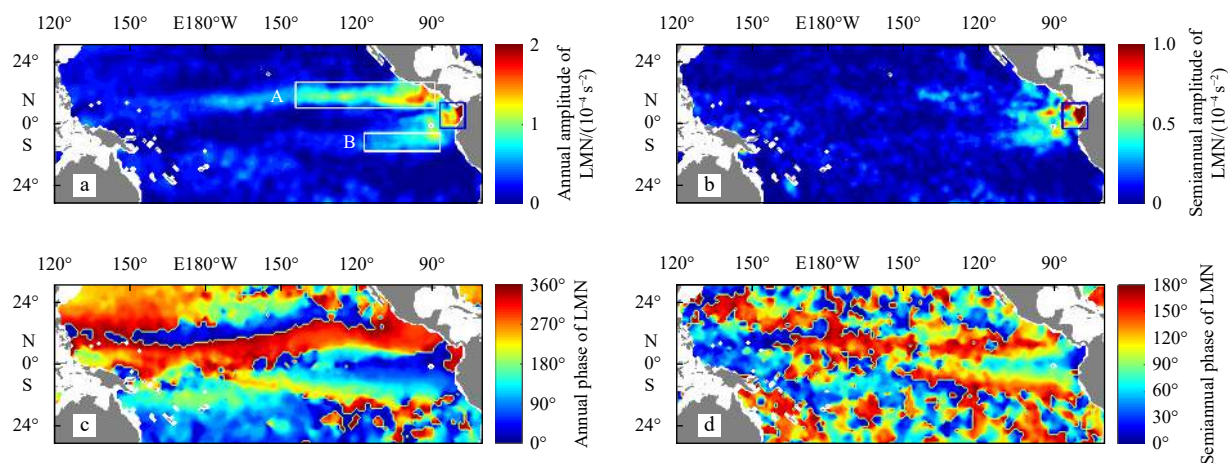
Fig. 9. Amplitude of the annual (a) and semiannual variations (b) in the LMN, and phases of the annual (c) and semiannual variations (d) in the LMN corresponding to the day of the year when the LMN is at a maximum for the period January 2004 to December 2017. White boxes in a indicate Region A (6°–16°N, 145°–90°W) and Region B (10°–3°S, 118°–88°W), respectively. Blue box in a and b indicate the Panama Bight region.
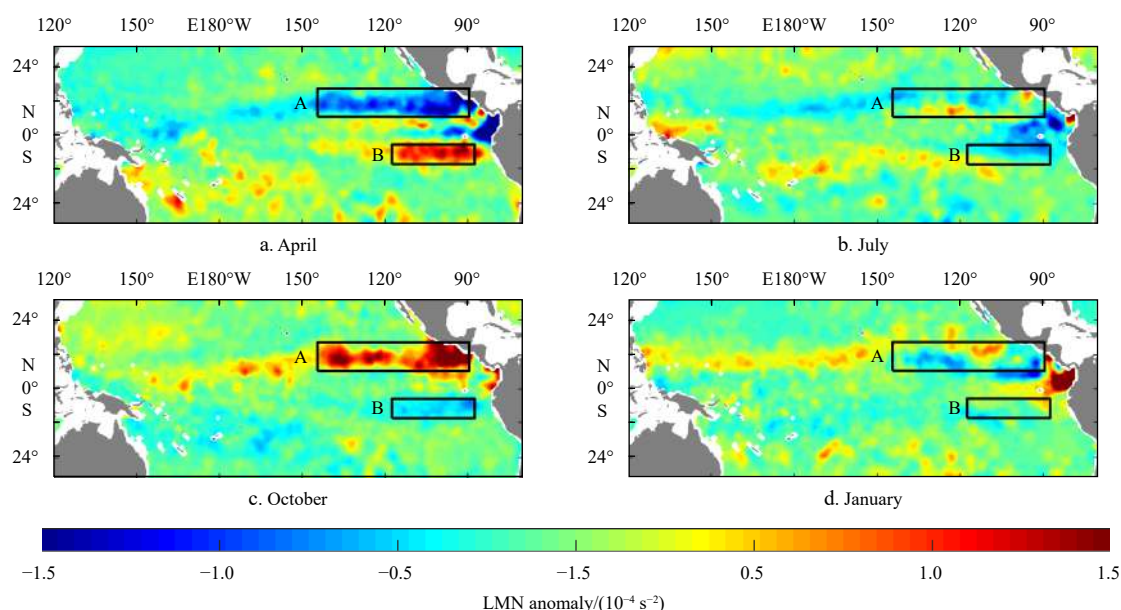
Fig. 10. Spatial distribution of the LMN anomaly relative to the long-term (2004–2017) mean in April (a), July (b), October (c) and January (d). Black boxes indicate Region A (6°–16°N, 145°–90°W) and Region B (10°–3°S, 118°–88°W), respectively.

with a large negative (positive) LMN anomaly in April (October) over Region A. There is an obvious seesaw pattern between the Region A and Region B, with smaller amplitude in Region B.
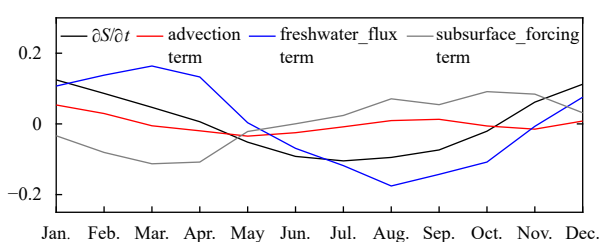
Different physical processes may be responsible for the seasonal evolution of salinity stratification. A mixed-layer salinity budget was used to diagnose the processes that controlled the seasonal variations. Seasonal cycles of each term in Eq. (1) in Region A are shown in Fig. 11 by removing their annual mean values. The mixed layer salinity tendency is negative during April and October. The accumulative mixed layer salinity decreasing forms a salinity minimum in October over Region A, which is well represented in Fig. 10c as a large positive LMN anomaly. During October to April, mixed layer salinity in Region A increases continually and gets it maximum in April. That explains why a remarkable negative LMN anomaly exists in April over Region A (Fig. 10a).

The most consistent tendency with the mixed layer salinity tendency is the freshwater flux term, which has a negative anomaly from May to October (Fig. 11). The accumulated freshwater inputs freshen the surface water continually in Region A and form the large positive LMN anomaly in October. The freshwater flux term shows a contrasting pattern from November to following April, thereby salinizing sea surface and generating a negative LMN anomaly in April. These results indicate the direct role of freshwater flux on the surface layer salinity, as described by Zhi et al. (2015). The likely possible mechanism that accounts for the seasonal variations of freshwater flux is the south-north immigration of the ITCZ and the accompanying movement of the rainfall center in the North Hemisphere.

Previous studies have illustrated that freshwater flux forcing can explain the variations in salinity to some extent but not completely (Qu et al., 2011; Du et al., 2019), ocean dynamics control the rest of salinity variation. The subsurface forcing term has a positive anomaly from June to October and negative anomaly from January to April, which restrains the freshening effect of the freshwater flux term (Fig. 11). Compared to the former two terms, seasonal cycle of horizontal advection term in Region A is much weaker.

4.2 *Interannual variability*

The global climate phenomenon, El Niño Southern Oscillation, occurs in the study region, and it may have an impact on salinity stratification. The spatial distribution of the correlation coefficient between the LMN and the Niño 3.4 index is provided in Fig. 12a. The LMN has a positive correlation with Niño 3.4 over the western-central equatorial Pacific around the dateline and negative correlations in the southwestern and northwestern tropical Pacific. In the eastern Pacific, their correlation is not signific-

ant. This pattern is consistent with the regression coefficients of SSS with the Niño-S34.8 index in Qu and Yu (2014) (see their Fig. 4b), which indicates the importance of SSS in regulating the upper-ocean salinity stratification. Nevertheless, the relationship between salinity stratification and ENSO events is somewhat different from SSS and ENSO. ENSO affects salinity stratification only in the western-central Pacific, while ENSO influences SSS in the eastern Pacific as well. The differences show the influence of subsurface salinity on salinity stratification in the eastern Pacific with relatively shoal halocline. Figure 12b shows the time series of the normalized regionally averaged LMN and Niño 3.4 index in the western-central equatorial Pacific (Fig.12a, black box). Positive LMN anomaly exists in all El Niño years (2004/2005, 2006/2007, 2009/2010, 2015/2016) and the correlation coefficient between LMN and Niño 3.4 index in this region can reach 0.72.

Figure 13a shows the Hovmöller diagram of the LMN anomaly with the seasonal cycle removed within the equatorial band (2.5°S–2.5°N). In the western-central equatorial Pacific, the LMN anomaly shows a good correlation with ENSO. During the winters of 2004, 2006, 2009 and 2015, when El Niño reached its mature phase (Fig. 13e), a large positive LMN anomaly occurred along the eastern edge of the warm pool. In the mature phase of the 2015/2016 extreme El Niño, this positive salinity stratification anomaly became more distinct. During La Niña events, a negative anomaly of LMN occurred in the same region.

Figures 13b–d show the Hovmöller diagram of the *E–P* anomaly, thermocline depth (considered as 20°C isotherm depth, Z20) anomaly and zonal wind anomaly with their seasonal cycle removed within the equatorial band (2.5°S–2.5°N). During El Niño events, atmospheric convection center moves eastward so strong freshwater anomaly is occurred in the western-central equatorial
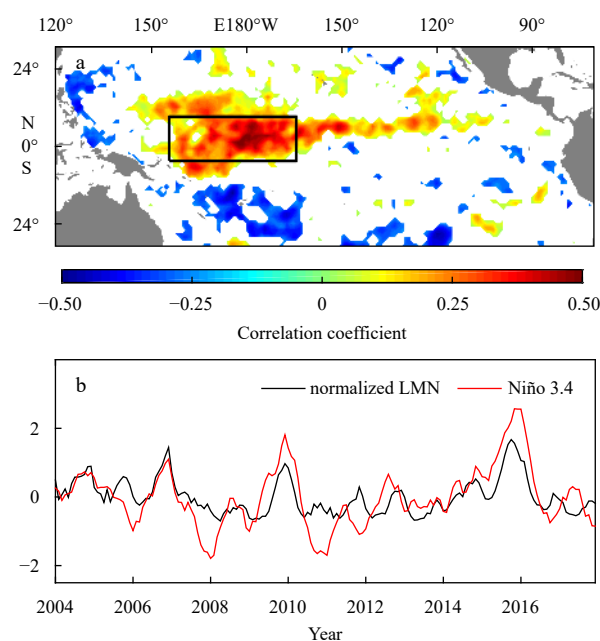
Fig. 12. Spatial distribution of the correlation coefficient between Niño 3.4 and normalized LMN (a), and time series of the regionally averaged normalized LMN in western-central equatorial Pacific (4°S–10°N, 155°E–165°W; black box in a) and the Niño 3.4 index during 2004–2017 (b). In a, the correlation coefficients which are not significant at the 95% confidence level are not shown.


Fig. 11. Seasonal cycles of the regionally averaged $\partial S/\partial t$ (psu/month), advection term, freshwater flux term and subsurface forcing term anomaly in Region A (6°–16°N, 145°–90°W) relative to their long-term mean value.

Pacific (Qu et al., 2014; Zhi et al., 2015), which freshened the upper ocean and increased the vertical salinity gradient (Fig. 13b). In addition to the freshwater forcing, SSS front in this region will move eastward and spread the fresh pool due to the horizontal advection during El Niño (Bosc et al., 2009). Moreover, thermocline shoals during El Niño in the western-central equatorial Pacific and brought saltier water upward to the subsurface (Fig. 13c). The joint role of surface freshening and subsurface salting caused this strong positive salinity stratification anomaly. The westerly wind anomaly in the central Pacific accounts for the thermocline fluctuations during El Niño by driving eastward downwelling Kelvin waves and westward upwelling Rossby waves (Fig. 13d).

4.3 *Interannual variability in the baroclinic gravity-wave phase speed*

The propagation velocity of gravity wave in the tropical Pacific is well related to ocean stratification. The gravity wave speed can be calculated as follows:

$$C_n = \frac{1}{n\pi} \int_{-H}^{0} N(z)\,\mathrm{d}z, \tag{5}$$

where C_n is the phase speed of the n-th baroclinic gravity wave (Chelton et al., 1998; Cai et al., 2008), H is the water depth and N is the Brunt-Väisälä frequency. In this study, the first baroclinic gravity wave phase speed C_1 is derived using global Argo gridded data and WOA13 seasonal climatology data.

Figure 14a shows the spatial distribution of long-term mean C_1, which shows a spatial difference in the tropical Pacific, with faster speeds in the west and slower speeds in the east. Both vertical stratification and water depth differences are responsible for this spatial discrepancy. Since N can be separated into temperature and salinity, the salinity part of the first baroclinic gravity
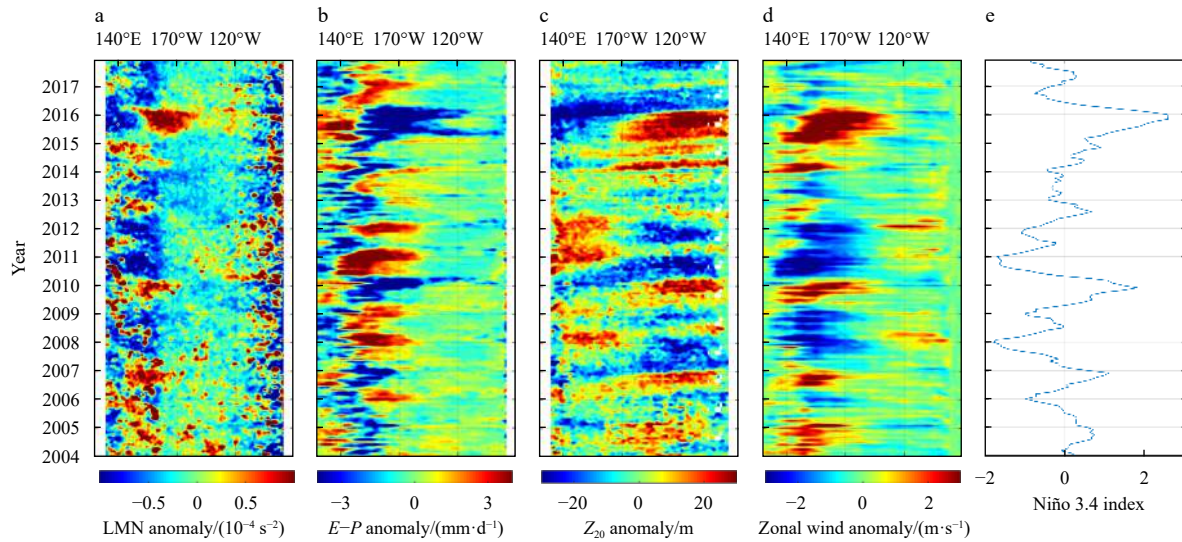
Fig. 13. Hovmöller diagrams of the LMN anomaly (a), E–P anomaly (b), 20°C isotherm depth anomaly (Z_{20}, c) and zonal wind anomaly (d) during the period of 2004–2017 with seasonal cycles removed within the equatorial band (2.5°S–2.5°N), and Niño 3.4 index for the period 2004 to 2017 (e).
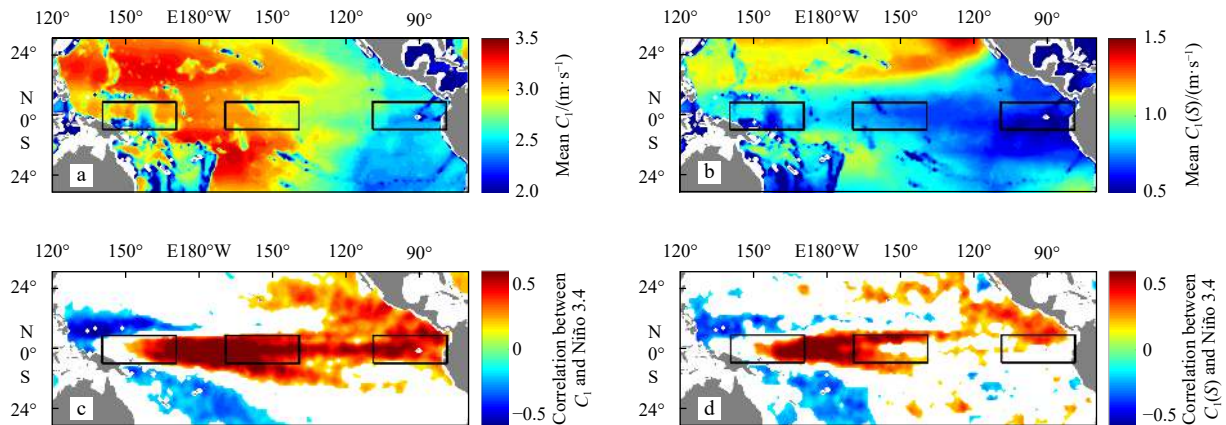

Fig. 14. Spatial distribution of the climatological mean C_1 (a) and $C_1(S)$ (b), spatial distribution of the correlation coefficient between C_1 and the Niño 3.4 index (c) and between $C_1(S)$ and the Niño 3.4 index (d). Black boxes from left to right are zoned as western Pacific, central Pacific and eastern Pacific, respectively. Correlation coefficients which are not significant at the 95% confidence level are not shown.

wave phase speed ($C_1(S)$ hereafter) is also calculated (Fig. 14b). $C_1(S)$ is only a fraction of C_1 in the equatorial region considering the dominant temperature feature at low latitudes.

Interannual variability in C_1 and $C_1(S)$ are presented here by considering their relationships with El Niño. It is evident that the propagation of the first baroclinic gravity wave is well influenced by El Niño. C_1 increases along the equatorial Pacific and decreases over the far western tropical Pacific during El Niño events (Fig. 14c). The correlation between $C_1(S)$ and Niño 3.4 index are similar to which between LMN and Niño 3.4 index (Figs 12a and 14d), indicating that the interannual variation of LMN can affect $C_1(S)$ to some extent.

Figure 15 gives the time series of phase speed in the western Pacific (5°S–5°N, 140°–170°E), central Pacific (5°S–5°N, 170°–140°W) and eastern Pacific (5°S–5°N, 110°–80°W) (black boxes in Fig. 14). It can be observed that salinity stratification plays an important role in the interannual variability of gravity wave speed over the western Pacific (Fig. 15a). With eastward progression, temperature stratification gradually dominates this impact (Figs 15b and c). In the central Pacific Ocean, a strong interannual signal with an ENSO-like pattern is observed (Fig. 15b). During the 2015/2016 El Niño period, a relatively large positive anomaly of C_1 (~0.15 m/s) and $C_1(S)$ (~0.1 m/s) occurs during the mature phase of El Niño. In the eastern TPO, the magnitude of the $C_1(S)$ anomaly becomes very small, which means that the interannual variations in temperature stratification instead of salinity stratification dominate the variability of the first baroclinic gravity wave (Fig. 15c). The amplitude of the C_1 anomaly is less than 5% of the mean C_1, which is similar to that derived from NODC and LOC data in Chelton et al. (1998).
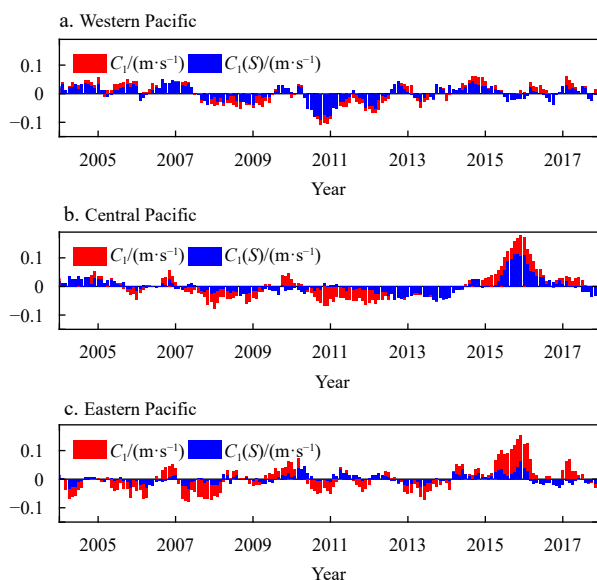
Fig. 15. Time series of the C_1 (red bar) anomaly and $C_1(S)$ (blue bar) anomaly in the western Pacific (a, left black box in Fig. 14) central Pacific (b, middle black box in Fig. 14) and eastern Pacific Ocean (c, right black box in Fig. 14). All seasonal cycles are removed.

5 Summary

Long-term gridded Argo dataset provides a good opportunity for us to describe the spatial and temporal variability in salinity stratification in the tropical Pacific Ocean. From the point of views of climatology, seasonal variation and interannual variation, some interesting conclusions are obtained.

Generally, salinity is low in the northern TPO and high in the southern TPO. The hemispheric discrepancy in salinity in the upper layer is primarily due to the difference in evaporation and precipitation between the two hemispheres. Salinity has a vertical maximum at the subsurface in the TPO with a depth of approximately 100–150 m. The role of salinity stratification is especially important among the total ocean stratification in the upper layer of the western Pacific Ocean, where a thick barrier layer exists.

Salinity stratification is specifically quantified as the LMN and HD in this investigation. LMN and HD have opposite spatial pattern in climatology, with large LMN and shallow HD exist in the western Pacific warm pool and eastern Pacific fresh pool. The LMN varies significantly in the upper layer and shows an obvious seasonal cycle in the north side of eastern equatorial Pacific. The freshwater flux forcing plays a crucial role in these seasonal variations, followed by the subsurface forcing. Interannual variability in salinity stratification associated with ENSO is significant in the western-central equatorial Pacific. Precipitation anomaly associated with the thermocline shoaling by the westerly wind anomaly lead to the salinity stratification anomaly. Interannual variations in ocean stratification can slightly affect the first baroclinic gravity-wave phase speed.

Salinity are received more and more attentions recently. In fact, there are many discrepancies between ocean temperature and ocean salinity. Despite both salinity and temperature vary with atmospheric forcing, their mechanisms are quite different. The heat content and SST can interact with atmospheric convection through a coupled process. However, the change in salinity stratification has no direct impact on the atmosphere, while feedback among salinity stratification, SST and precipitation does. Therefore, the influence of atmospheric forcing on salinity stratification is nonreversible, which is an important insight. There are many potential discoveries in ocean salinity from both dynamic and thermodynamic perspectives. Understanding the characteristics of upper-ocean salinity stratification may help improving the simulation of many other processes in ocean-atmosphere coupled models in the foreseeable future.

References

Adler R F, Sapiano M, Huffman G J, et al. 2018. The global precipitation climatology project (GPCP) monthly analysis (new version 2.3) and a review of 2017 global precipitation. Atmosphere, 9(4): 138, doi: 10.3390/atmos9040138

Alory G, Maes C, Delcroix T, et al. 2012. Seasonal dynamics of sea surface salinity off Panama: The far eastern Pacific fresh pool.

Journal of Geophysical Research: Oceans, 117(C4): C04028, doi: 10.1029/2011JC007802

Bonjean F, Lagerloef G S E. 2002. Diagnostic model and analysis of the surface currents in the Tropical Pacific Ocean. Journal of Physical Oceanography, 32(10): 2938–2954, doi: 10.1175/1520-0485(2002)032<2938:DMAAOT>2.0.CO;2

Bosc C, Delcroix T, Maes C. 2009. Barrier layer variability in the western Pacific warm pool from 2000 to 2007. Journal of Geophysical Research: Oceans, 114(C6): C06023, doi: 10.1029/2008JC005187

Cai Shuqun, Long Xiaomin, Wu Renhao, et al. 2008. Geographical and monthly variability of the first baroclinic Rossby radius of deformation in the South China Sea. Journal of Marine Systems, 74(1–2): 711–720

Chelton D B, deSzoeke R A, Schlax M G, et al. 1998. Geographical variability of the first baroclinic Rossby radius of deformation. Journal of Physical Oceanography, 28(3): 433–460, doi: 10.1175/1520-0485(1998)028<0433:GVOTFB>2.0.CO;2

Chen Ge, Peng Lin, Ma Chunyong. 2018. Climatology and seasonality of upper ocean salinity: A three-dimensional view from Argo floats. Climate Dynamics, 50(5–6): 2169–2182, doi: 10.1007/s00382-017-3742-6

Chi Jingshan, Du Yan, Zhang Yuhong, et al. 2019. A new perspective of the 2014/15 failed El Niño as seen from ocean salinity. Scientific Reports, 9: 2720, doi: 10.1038/s41598-019-38743-z

Chu P C, Fan Chenwu. 2011. Maximum angle method for determining mixed layer depth from seaglider data. Journal of Oceanography, 67(2): 219–230, doi: 10.1007/s10872-011-0019-2

Delcroix T, Hénin C. 1991. Seasonal and interannual variations of sea surface salinity in the tropical Pacific Ocean. Journal of Geophysical Research: Oceans, 96(C12): 22135–22150, doi: 10.1029/91JC02124

Delcroix T, McPhaden M. 2002. Interannual sea surface salinity and temperature changes in the western Pacific warm pool during 1992–2000. Journal of Geophysical Research: Oceans, 107(C12): SRF 3-1–SRF 3-17, doi: 10.1029/2001JC000862

Du Yan, Zhang Yuhong, Feng Ming, et al. 2015. Decadal trends of the upper ocean salinity in the tropical Indo-Pacific since mid-1990s. Scientific Reports, 5: 16050, doi: 10.1038/srep16050

Du Yan, Zhang Yuhong, Shi Jiancheng. 2019. Relationship between sea surface salinity and ocean circulation and climate change. Science China Earth Sciences, 62(5): 771–782, doi: 10.1007/s11430-018-9276-6

Entekhabi D, Njoku E G, O'Neill P E, et al. 2010. The soil moisture active passive (SMAP) mission. Proceedings of the IEEE, 98(5): 704–716, doi: 10.1109/JPROC.2010.2043918

Feng Ming, Hacker P, Lukas R. 1998. Upper ocean heat and salt balances in response to a westerly wind burst in the western equatorial Pacific during TOGA COARE. Journal of Geophysical Research: Oceans, 103(C5): 10289–10311, doi: 10.1029/97JC03286

Font J, Camps A, Borges A, et al. 2010. SMOS: The challenging sea surface salinity measurement from space. Proceedings of the IEEE, 98(5): 649–665, doi: 10.1109/JPROC.2009.2033096

Gasparin F, Roemmich D. 2016. The strong freshwater anomaly during the onset of the 2015/2016 El Niño. Geophysical Research Letters, 43(12): 6452–6460, doi: 10.1002/2016GL069542

Godfrey J S, Lindstrom E J. 1989. The heat budget of the equatorial western Pacific surface mixed layer. Journal of Geophysical Research: Oceans, 94(C6): 8007–8017, doi: 10.1029/JC094iC06p08007

Guan Cong, Hu Shijian, McPhaden M J, et al. 2019. Dipole structure of mixed layer salinity in response to El Niño-La Niña asymmetry in the tropical Pacific. Geophysical Research Letters, 46(21): 12165–12172, doi: 10.1029/2019GL084817

Guimbard S, Reul N, Chapron B, et al. 2017. Seasonal and interannual variability of the eastern tropical pacific fresh pool. Journal of Geophysical Research: Oceans, 122(3): 1749–1771, doi: 10.1002/2016jc012130

Hasson A E A, Delcroix T, Dussin R. 2013. An assessment of the mixed layer salinity budget in the tropical Pacific Ocean. Observations and modelling (1990–2009). Ocean Dynamics, 63(2–3): 179–194

Helber R W, Kara A B, Richman J G, et al. 2012. Temperature versus salinity gradients below the ocean mixed layer. Journal of Geophysical Research: Oceans, 117(C5): C05006, doi: 10.1029/2011JC007382

Kao H Y, Lagerloef G S. 2015. Salinity fronts in the tropical Pacific Ocean. Journal of Geophysical Research: Oceans, 120(2): 1096–1106, doi: 10.1002/2014JC010114

Lagerloef G, Colomb F R, Le Vine D, et al. 2008. The Aquarius/SAC-D mission: Designed to meet the salinity remote-sensing challenge. Oceanography, 21(1): 68–81

Lorbacher K, Dommenget D, Niiler P P, et al. 2006. Ocean mixed layer depth: A subsurface proxy of ocean-atmosphere variability. Journal of Geophysical Research: Oceans, 111(C7): C07010

Lu Shaolei, Liu Zenghong, Li Hong, et al. 2020. User Manual Of Global Ocean Argo Gridded Datasets (BOA_Argo) (in Chinese). Hangzhou: China Argo Real-Time Data Center, 28

Lukas R, Lindstrom E. 1991. The mixed layer of the western equatorial Pacific Ocean. Journal of Geophysical Research: Oceans, 96(S01): 3343–3357, doi: 10.1029/90JC01951

Maes C. 2008. On the ocean salinity stratification observed at the eastern edge of the equatorial Pacific warm pool. Journal of Geophysical Research: Oceans, 113(C3): C03027, doi: 10.1029/2007JC004297

Maes C, O'Kane T J. 2014. Seasonal variations of the upper ocean salinity stratification in the Tropics. Journal of Geophysical Research: Oceans, 119(3): 1706–1722, doi: 10.1002/2013JC009366

McDougall T J. 1987. Neutral surfaces. Journal of Physical Oceanography, 17(11): 1950–1964, doi: 10.1175/1520-0485(1987)017<1950:NS>2.0.CO;2

O'Kane T J, Monselesan D P, Maes C. 2016. On the stability and spatiotemporal variance distribution of salinity in the upper ocean. Journal of Geophysical Research: Oceans, 121(6): 4128–4148, doi: 10.1002/2015JC011523

Qu Tangdong, Gao Shan, Fine R A. 2013. Subduction of South Pacific tropical water and its equatorward pathways as shown by a simulated passive tracer. Journal of Physical Oceanography, 43(8): 1551–1565, doi: 10.1175/jpo-d-12-0180.1

Qu Tangdong, Gao Shan, Fukumori I. 2011. What governs the North Atlantic salinity maximum in a global GCM?. Geophysical Research Letters, 38(7): L07602, doi: 10.1029/2011GL046757

Qu Tangdong, Song Y T, Maes C. 2014. Sea surface salinity and barrier layer variability in the equatorial Pacific as seen from Aquarius and Argo. Journal of Geophysical Research: Oceans, 119(1): 15–29, doi: 10.1002/2013JC009375

Qu Tangdong, Yu Jinyi. 2014. ENSO indices from sea surface salinity observed by Aquarius and Argo. Journal of Oceanography, 70(4): 367–375, doi: 10.1007/s10872-014-0238-4

Roemmich D, Johnson G C, Riser S, et al. 2009. The Argo Program: observing the Global Ocean with profiling floats. Oceanography, 22(2): 34–43

Simmons A, Uppala S, Dee D, et al. 2006. ERA-Interim: New ECMWF reanalysis products from 1989 onwards. ECMWF Newsletter, 110: 26–35

Singh A, Delcroix T, Cravatte S. 2011. Contrasting the flavors of El Niño-Southern Oscillation using sea surface salinity observations. Journal of Geophysical Research: Oceans, 116(C6): C06016, doi: 10.1029/2010JC006862

Sprintall J, Tomczak M. 1992. Evidence of the barrier layer in the surface layer of the tropics. Journal of Geophysical Research: Oceans, 97(C5): 7305–7316, doi: 10.1029/92JC00407

Vialard J, Delecluse P. 1998. An OGCM study for the TOGA decade. Part II: Barrier-layer formation and variability. Journal of physical oceanography, 28(6): 1089–1106, doi: 10.1175/1520-0485(1998)028<1089:AOSFTT>2.0.CO;2

Wang Xidong, Liu Hailong. 2016. Seasonal-to-interannual variability of the barrier layer in the western Pacific warm pool associated with ENSO. Climate Dynamics, 47(1–2): 375–392, doi: 10.1007/s00382-015-2842-4

Xie Shangping. 1999. A dynamic ocean-atmosphere model of the

Tropical Atlantic decadal variability. Journal of Climate, 12(1): 64–70, doi: 10.1175/1520-0442-12.1.64

Xie Shangping. 2004. The shape of continents, air-sea interaction, and the rising branch of the Hadley Circulation. In: Diaz H F, Bradley R S, eds. The Hadley Circulation: Present, Past and Future. Dordrecht: Springer, 121–152, doi: 10.1007/978-1-4020-2944-8_5

Xie Shangping, Xu Haiming, Kessler W S, et al. 2005. Air-sea interaction over the eastern Pacific warm pool: Gap winds, thermocline dome, and atmospheric convection. Journal of Climate, 18(1): 5–20, doi: 10.1175/JCLI-3249.1

Yu Lisan. 2011. A global relationship between the ocean water cycle and near-surface salinity. Journal of Geophysical Research: Oceans, 116(C10): C10025, doi: 10.1029/2010JC006937

Yu Lisan, Jin Xiangze, Weller R A. 2008. Multidecade global flux datasets from the objectively analyzed air-sea fluxes (OAFlux) Project: latent and sensible heat fluxes, ocean evaporation, and related surface meteorological variables. Massachusetts: Woods Hole Oceanographic Institution, 64

Zheng Fei, Zhang Ronghua. 2012. Effects of interannual salinity variability and freshwater flux forcing on the development of the 2007/08 La Niña event diagnosed from Argo and satellite data. Dynamics of Atmospheres and Oceans, 57: 45–57, doi: 10.1016/j.dynatmoce.2012.06.002

Zhi Hai, Zhang Ronghua, Lin Pengfei, et al. 2015. Quantitative analysis of the feedback induced by the freshwater flux in the tropical Pacific using CMIP5. Advances in Atmospheric Sciences, 32(10): 1341–1353, doi: 10.1007/s00376-015-5064-0

Zhi Hai, Lin Pengfei, Zhang Ronghua, et al. 2019a. Salinity effects on the 2014 warm "Blob" in the Northeast Pacific. Acta Oceanologica Sinica, 38(9): 24–34, doi: 10.1007/s13131-019-1450-2

Zhi Hai, Zhang Ronghua, Lin Pengfei, et al. 2019b. Interannual salinity variability in the tropical Pacific in CMIP5 simulations. Advances in Atmospheric Sciences, 36(4): 378–396, doi: 10.1007/s00376-018-7309-1

Zhi Hai, Zhang Ronghua, Lin Pengfei, et al. 2019c. Effects of salinity variability on recent El Niño events. Atmosphere, 10(8): 475, doi: 10.3390/atmos10080475